Net northward ocean heat transport modulates hemispheric cloud asymmetries

Aiden Jönsson[*,1,2], Frida Bender[1,2], Thorsten Mauritsen[1,2], and Rodrigo Caballero[1,2]

[1]Department of Meteorology, Stockholm University, Stockholm, Sweden

[2]The Bolin Centre for Climate Research, Stockholm University, Stockholm, Sweden

[*]Correspondence: aiden.jonsson@misu.su.se

ABSTRACT

Clouds in the Southern Hemisphere (SH) extratropics make up for the Northern Hemisphere (NH)'s greater tropical cloud cover and clear-sky albedo, making Earth's planetary albedo hemispherically symmetric over the satellite record. Knowledge of a mechanism for maintaining hemispheric albedo symmetry would prove valuable for understanding cloud responses to external forcings. Using simulations of an Earth-like aquaplanet, we investigate the role of ocean heat transport (OHT) in determining hemispheric differences in cloud cover. With increasing northward cross-equatorial OHT, the SH becomes dominant in low cloud cover at all latitudes, while NH increases in high clouds are negated by reductions in low clouds. We describe a dynamical link between the increasing SH extratropical cloud cover and increasing NH tropical cloud cover with more northward cross-equatorial OHT. We investigate the effects of clouds and condensation on AHT responses, which increase southward AHT through latent heating in the extratropics and radiative effects in lower latitudes, aiding in reducing the hemispheric energy contrast. Because SH cloud increases are greater than NH cloud reductions, increasing cloud asymmetry with more northward cross-equatorial OHT leads to net increases in global cloud cover and cooling.

Keywords: Clouds, albedo symmetry, atmospheric circulation, heat transport

1 INTRODUCTION

Earth's Northern and Southern Hemispheres (NH and SH, respectively) have substantial differences in cloud cover, a feature that makes Earth's observed symmetry between NH and SH planetary albedo possible despite differences in clear-sky albedo stemming from having more aerosol emissions and land surface area (Voigt et al., 2013; Stephens et al., 2015; Datseris and Stevens, 2021; Diamond et al., 2022). The primary compensating features provided by clouds are greater cloud amount in the SH subtropics, and greater cloud amount and albedo in the SH midlatitudes (Bender et al., 2017; Blanco et al., 2023). Compensating differences in cloud cover and properties occur almost exclusively over ocean, normalized over area (Datseris and Stevens, 2021). This hemispheric albedo symmetry has persisted for over two decades despite global changes in albedo (Jönsson and Bender, 2022).

Identification of a physical mechanism imposing hemispheric albedo symmetry remains elusive, but it has been speculated that it would provide constraints for predicting cloud cover and its features across climate states (Stevens and Schwartz, 2012; Voigt et al., 2013; Stephens et al., 2015), and thus on shortwave (SW) cloud radiative feedbacks. One proposed mechanism is the location of the tropical maximum in cloud cover that occurs at the intertropical convergence zone (ITCZ), which would shift into a darker hemisphere due to the increase in atmospheric

heating (Kang et al., 2008; Voigt et al., 2014). However, its average northerly position currently reinforces asymmetry (Bender et al., 2017). Its shift relative to pre-industrial conditions may play a small role in maintaining albedo symmetry with greenhouse gas (GHG)-induced warming, but cannot sufficiently compensate for projected NH darkening that would result from Arctic warming (Jönsson and Bender, 2023). Instead, climate models provide evidence that midlatitude differences in cloud cover have a strong potential to drive mean-state albedo symmetry, as they are the primary cause of model albedo asymmetry biases (Jönsson and Bender, 2022). While subtropical clouds are predicted to contribute heavily to SW cloud radiative feedbacks (Myers and Norris, 2015; Zelinka et al., 2016; Schiro et al., 2022), their role in the hemispheric albedo symmetry has not been investigated in depth.

Hemispheric differences in midlatitude cloud cover are to a large part determined by hemispheric asymmetries in storm track intensity (Blanco et al., 2023; Hadas et al., 2023). The hemispheric difference in storm track intensity is to a large extent explained by differences in poleward ocean heat transport (OHT) in each hemisphere's midlatitudes; poleward atmospheric heat transport (AHT) by eddies reduces in the NH in response to stronger poleward OHT, since OHT reduces the meridional temperature gradient (Shaw et al., 2022). These links to ocean dynamics have implications for the evolution of the albedo symmetry and cloud cover during global warming; climate models that recover their pre-industrial albedo asymmetry in GHG-forced warming experiments do so through ocean-driven losses of SH midlatitude clouds (Jönsson and Bender, 2023). Underlining the role of the ocean in controlling albedo symmetry, hemispheric temperature contrasts and their warming responses are linked to albedo asymmetries and their warming responses across climate models (Rugenstein and Hakuba, 2023); the hemispheric temperature contrast itself is primarily caused by a net northward cross-equatorial OHT (Kang et al., 2015).

Here we seek to better understand the role of northward cross-equatorial OHT in driving global features of cloud cover, which is key to predicting the evolution of the hemispheric albedo symmetry and cloud cover. Using idealized simulations in Earth-like aquaplanets, we investigate the links between clouds and large-scale atmospheric circulation responses to hemispheric asymmetries in ocean heat convergence, and explore whether it is possible to reproduce the observed hemispheric differences in clouds using OHT.

2 METHODS AND MATERIALS

We use the Community Atmosphere Model version 6 (CAM6), the atmospheric component of the Community Earth System Model, version 2.1.0 (Danabasoglu et al., 2020), in the aquaplanet configuration with a slab ocean model (QSC6 component set) at $1.9° \times 2.5°$ resolution. We use present-day obliquity, rotation rates, orbital parameters, solar constant, and an atmospheric composition with a CO_2 volume mixing ratio is 367 ppm(v) (F2000climo settings). Only sea salt emissions are treated, and there is no sea ice component.

2.1 Experimental design

The control simulation's meridional profile of ocean heat fluxes (Q) as a function of latitude (φ) are determined to match surface energy fluxes from a 5-year fixed-SST simulation with a prescribed "QOBS" (Neale and Hoskins, 2000) idealized zonally symmetric meridional SST profile. The fluxes from this simulation were averaged for each equivalent latitude in both hemispheres and mirrored across the equator to ensure a symmetric control Q-flux profile. Anomalous heat fluxes Q' are added to the control Q-fluxes with varying amplitudes A, emulating

84 ocean heat divergence in the SH and convergence in the NH, with the form of:

$$Q'(\varphi) = -A \cdot \sin(\varphi). \tag{1}$$

85 Current estimates of the net cross-equatorial OHT are ∼0.4-0.5 PW (Loeb et al., 2016). Steps
86 of $A = 2$ W m^{-2} yield increments of cross-equatorial OHT (XOHT) of ∼0.25 PW; we perform
87 simulations with XOHT up to 1.27 PW (Figure 1). In a coupled setting, ocean dynamics would
88 respond to hemispheric asymmetries in heating and provide a significant portion of the total
89 cross-equatorial OHT, ultimately dampening the magnitude of atmospheric circulation responses
90 (Green et al., 2019). Since our simulations do not have dynamic oceans, we do not expect our
91 simulations to quantitatively liken real responses of the atmosphere to cross-equatorial OHT, and
92 focus on the processes driving atmospheric circulation and cloud responses to northward XOHT.

2.2 Heat transport calculations

94 We calculate any meridional heat transport HT(φ) by spatially integrating a flux profile ● (φ)
95 over a polar cap southward of the latitude φ:

$$\mathrm{HT}(\varphi) = 2\pi a^2 \int_{-\pi/2}^{\varphi} \bullet \, (\varphi) \cos(\varphi) \, d\varphi, \tag{2}$$

96 where a is the radius of Earth (Liu et al., 2017). OHT is the heat transport implied by the
97 ocean heat flux profile and is calculated with (2) using ● (φ) $= Q(\varphi)$. The total MHT of the
98 atmosphere-ocean system is calculated using the TOA energy balance in equation (2):

$$\mathrm{MHT}(\varphi) = 2\pi a^2 \int_{-\pi/2}^{\varphi} \big(\mathrm{ASR}(\varphi) - \mathrm{OLR}(\varphi)\big) \cos(\varphi) \, d\varphi. \tag{3}$$

99 Atmospheric heat transport (AHT) is then the difference between MHT and OHT:

$$\mathrm{AHT}(\varphi) = \mathrm{MHT}(\varphi) - \mathrm{OHT}(\varphi), \tag{4}$$

100 where OHT(φ) is fixed by our experimental forcings. AHT is made up of meridional heat
101 transport of moist static energy (MSE) by mean meridional circulation (MMC) and transients.
102 MMC is calculated as:

$$\mathrm{MMC}(\varphi) = 2\pi a^2 \int_{-\pi/2}^{\varphi} \left(\int_{p_s}^{0} [v(p,\varphi)] \cdot [\mathrm{MSE}(p,\varphi)] \, dp \right) \cos(\varphi) \, d\varphi, \tag{5}$$

103 where brackets denote zonal time means and v is the meridional wind field. MSE is defined as:

$$\mathrm{MSE} = C_p \cdot T + L_v \cdot q + g \cdot \phi, \tag{6}$$

104 where C_p is the heat capacity of air, T is air temperature, L_v is the latent heat of vaporization,
105 q is specific humidity, g is the standard acceleration of gravity, and ϕ is the geopotential
106 height. Because our simulations are zonally symmetric, transient heat transport is dominated by
107 contributions from transient eddies (TE). We estimate TE using the residual AHT after MMC:

$$\mathrm{TE}(\varphi) = \mathrm{AHT}(\varphi) - \mathrm{MMC}(\varphi). \tag{7}$$

108 The total moist AHT is obtained by integrating the atmospheric moisture balance (evaporation E
109 minus precipitation P) field using equation (2):

$$\mathrm{AHT_M}(\varphi) = 2\pi a^2 \int_{-\pi/2}^{\varphi} L_v \cdot \big(\mathrm{E}(\varphi) - \mathrm{P}(\varphi)\big) \cos(\varphi) \, d\varphi. \tag{8}$$

110 Finally, AHT$_\mathrm{M}$ can be decomposed into moist contributions by MMC and TE (MMC$_\mathrm{M}$ and TE$_\mathrm{M}$,
111 respectively). MMC$_\mathrm{M}$ is obtained by replacing $[\mathrm{MSE}(p,\varphi)]$ with $[L_v \cdot q(p,\varphi)]$ in equation (5),
112 and TE$_\mathrm{M}$ is obtained by subtracting MMC$_\mathrm{M}$ from AHT$_\mathrm{M}$.
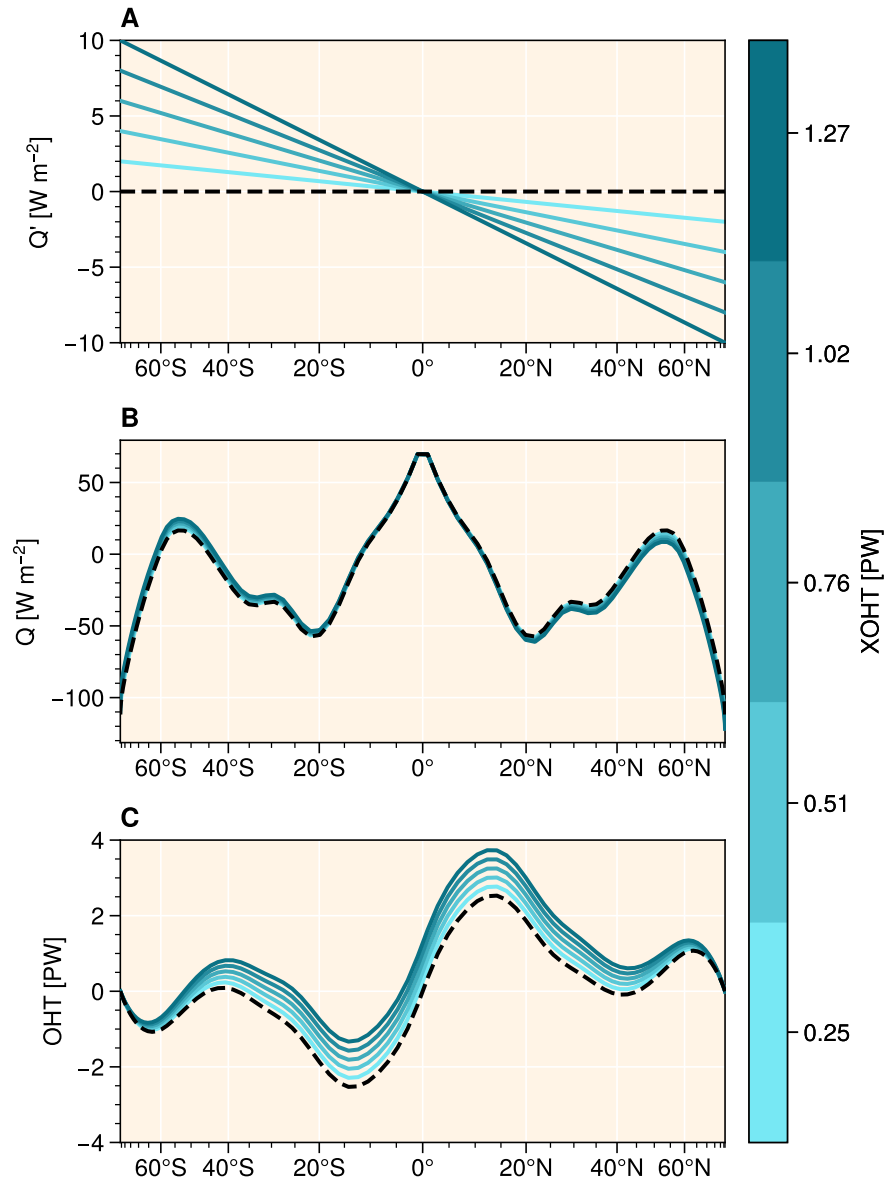
Figure 1. Meridional profiles of a) Q', b) Q, and c) OHT in the experimental design. The color of the line represents the magnitude of cross-equatorial OHT (XOHT) in each experiment. The dashed line represents the control (XOHT = 0 PW).

3 RESULTS

Our simulations exhibit global cooling with increasing XOHT (Figure 2e) due to an increase in global mean albedo and cloud cover (Figure 2f and h), which primarily stem from the SH. This implies nonlinearity in the cloud response to the imposed perturbation, despite the perturbation being exactly antisymmetric around the equator. Cloud albedo and thus absorbed solar radiation (ASR) are the primary drivers of hemispheric energetic asymmetries (we define Δ_H as the NH minus SH hemispheric mean difference of any field) across the simulations, with Δ_HASR ranging from roughly -1 to +26 W m^{-2}. Variations in hemispheric differences in outgoing longwave radiation (OLR) are slight, with Δ_HOLR ranging from roughly -4 to +5.5 W m^{-2} across the simulations. NH OLR begins increase after falling at XOHT > 0.76 PW (Figure 2g), likely due to the increase in OLR from low cloud loss outpacing reductions in OLR from increasing tropical high cloud cover. A key feature of the responses to our OHT forcings is that cloud fraction and albedo increases in the SH are not equal in magnitude to reductions in NH cloud cover. This feature aids in the ability of the global cloud distribution to maintain albedo symmetry, since smaller changes in cross-equatorial heat transport are needed to impart cloud albedo asymmetry. The first step of XOHT in our experimental design results in most of the variation across the simulations, indicating higher sensitivity of hemispheric asymmetries at lower XOHT. It is worth noting that the control simulation already exhibits asymmetry despite having symmetric surface heat fluxes; this asymmetry does not arise in simulations without present-day orbital eccentricity and longitude of perihelion, which may speak to a degree of control by orbitally forced hemispheric differences in the seasonal cycle (Roach et al., 2023).

The response of the cloud and reflectivity profile (Figure 2b) to increasing XOHT qualitatively captures the observed hemispheric differences–the NH has higher tropical cloud albedo, while the SH has higher subtropical and midlatitude cloud albedo (Bender et al., 2017; Blanco et al., 2023). The finding that SH extratropical cloud increases outpace NH tropical cloud increases mirrors previous experiments exploring the ability of the ITCZ to compensate for hemispheric clear-sky albedo asymmetries (Voigt et al., 2014). This is important to albedo symmetry; if the increase in one hemisphere's albedo when the ITCZ's mean position migrates into it were equal to the other hemisphere's albedo increase due to extratropical cloud cover, no compensation would be offered. In the following section, we will describe how the atmospheric circulation responses provide conditions for these cloud asymmetries.

3.1 Atmospheric circulation responses

Figure 3 illustrates the meridional and vertical variations in cloud cover and properties within our experiments: the maximum in tropical high cloud cover is in the NH, as one would expect from the increased convection due to the heat asymmetry in the tropics and the Hadley circulation response (Donohoe et al., 2013; Voigt et al., 2014). Extratropical asymmetries in cloud cover are primarily due to the dominance of SH low cloud cover at nearly all latitudes. Contrary to observations (Bodas-Salcedo et al., 2012, 2016), we do not find that SH midlatitude clouds have a larger liquid water to ice water content ratio than their NH counterparts in our simulations, although changes in LWP occur mostly in the upper range of mixed phase temperatures and LWP decreases are small relative to IWP increases (Figure 3); aerosols and the availability of ice-nucleating particles may play a role in this discrepancy with observed differences in cloud phase (Vergara-Temprado et al., 2018). In-cloud LWP increases in the NH midlatitudes with higher XOHT and is greater in the SH in all simulations. NH (SH) midlatitude cloud fraction declines (increases) with increasing XOHT. For stronger XOHT in our simulations, midlatitude cloud asymmetry primarily arises from NH cloud loss and not from SH increases in cloud cover as XOHT increases, and time-average cloud condensate is higher in the SH than the NH
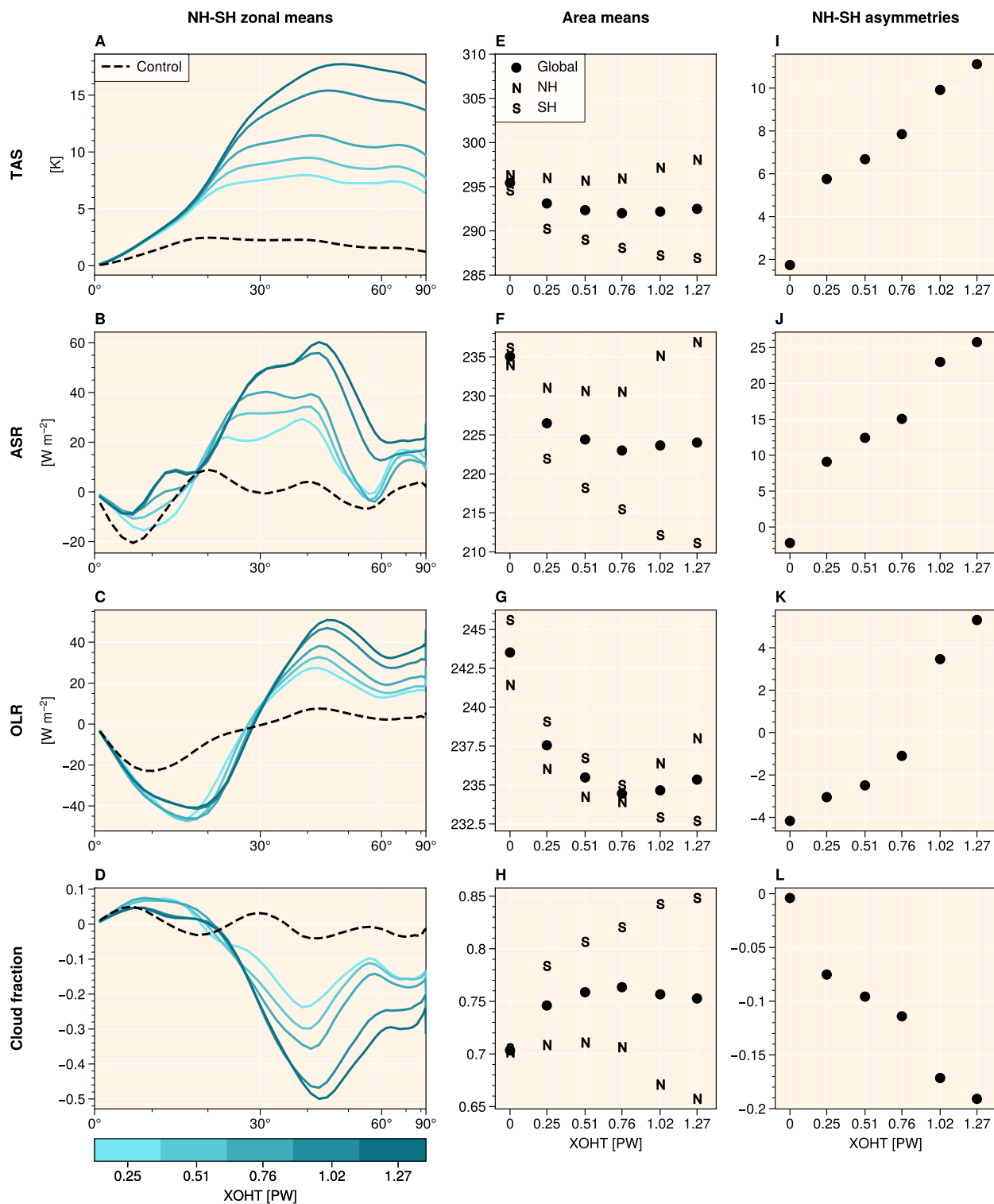
Figure 2. NH minus SH zonal mean (at each respective latitude) differences (first column), hemispheric and global means (second column), and NH minus SH hemispheric mean asymmetries (third column) for near-surface air temperature (TAS), absorbed solar radiation (ASR), outgoing longwave radiation (OLR), and cloud fraction. The color of each curve represents the simulation and amount of northward XOHT, and the dashed curve is the control simulation (XOHT = 0 PW).

160 midlatitudes primarily due to the cloud fraction asymmetry.

161 Hadley circulation responds to northward XOHT by shifting the rising branch into the warming
162 NH (see Supplementary Figure S1a-f). Crucially, the overturning strengths of the northern
163 and southern Hadley cells respond asymmetrically (Figure 4g). The southern cell stretches
164 over a larger meridional span and strengthens while the northern cell shrinks and weakens
165 (Supplementary Figure S1), resembling the climatological morphology of the observed Hadley
166 circulation (D'Agostino and Lionello, 2017). This provides a greater southward flow of warm
167 air aloft across the equator, increasing southward AHT (to be described in Section 4). In the
168 subtropics, hemispheric asymmetries in overturning strength provide stronger surface winds in
169 the southern cell and a deeper planetary boundary layer (PBL), while the greater overturning
170 strength and subsidence provides stronger lower tropospheric stability than the NH (Figure
171 4a-c). These asymmetries provide more favorable conditions for low cloud cover (LCC) in the
172 SH subtropics (Nuijens and Stevens, 2012; Klein et al., 2017). Thus, the immediate response
173 of overturning circulation to the hemispheric heat contrast reproduces the observed tropical
174 and subtropical cloud asymmetries, linking the NH dominance in high cloud cover and the SH
175 dominance in subtropical low cloud cover.

176 Midlatitude cloud albedo is tightly linked to the storm track intensity due to the upward mixing
177 of moisture provided by cyclones (Blanco et al., 2023; Hadas et al., 2023). Our simulations
178 display a stronger SH storm track, indicated by eddy kinetic energy (EKE) remaining strong in
179 the SH midlatitudes and declining in the NH (see Supplementary Figure S1g-l). With stronger
180 XOHT, the dynamically stormier SH provides the conditions for hemispheric midlatitude cloud
181 asymmetries that mirror the observed climatology (Bender et al., 2017; Shaw et al., 2022; Hadas
182 et al., 2023). While there is no consensus theory describing what determines storm track intensity,
183 the meridional temperature gradient is widely understood to be a key factor; this is reflected
184 by the increasing SH meridional gradient in DSE across the experiments (Figure 4i). The
185 strength of meridional flow in the upper Hadley cell branch is balanced by eddy momentum
186 flux divergence at the Hadley cell edge, linking midlatitude eddy activity and Hadley cell
187 strength (Walker and Schneider, 2006; Singh and Kuang, 2016; Davis and Birner, 2019), which
188 may provide a dynamical link between the tropics and extratropics that can affect hemispheric
189 cloud asymmetries. Although the northerly ITCZ's relation to the SH storm track position has
190 previously been explored (Ceppi et al., 2013), the link and direction of causal influence between
191 them is not well understood.

192 Midlatitude eddies act as the diffusive process providing poleward AHT in the extratropics,
193 mixing heat and moisture from low latitudes with colder, drier high-latitude air. Eddy diffusivity
194 is determined dynamically by characteristic velocity V and length scales L of eddies, and the
195 potential heat transport provided by eddies is determined by meridional gradients of temperature
196 and moisture. We estimate eddy diffusivity metrics using V estimated as the square root of the
197 mean square of instantaneous meridional velocities ($= \sqrt{\overline{vv}}$ where $\overline{vv}$ is the time average of
198 squared instantaneous v), and L as $\sqrt{2V/\beta}$, where β is the meridional gradient of the Coriolis
199 parameter. The product VL scales in proportion to the strength of eddy diffusivity (Barry et al.,
200 2002; Liu et al., 2017). Averages of these are taken over 30-60° in each hemisphere and presented
201 in Figure 4h. VL remains high in the SH midlatitudes, while it decreases in the NH midlatitudes.
202 This is consistent with the dynamically strong SH storm track and weakening NH storm track
203 seen in EKE across the experiments (Supplementary Figure S1g-l). This indicates that eddy
204 activity maintains a high potential for poleward heat transport in the SH. Poleward heat transport
205 is realized by acting on gradients of temperature and humidity; Figure 4i shows the magnitude
206 of meridional gradients in DSE and $L_v \cdot q$ across the eddy regions (30-60°) in each hemisphere.
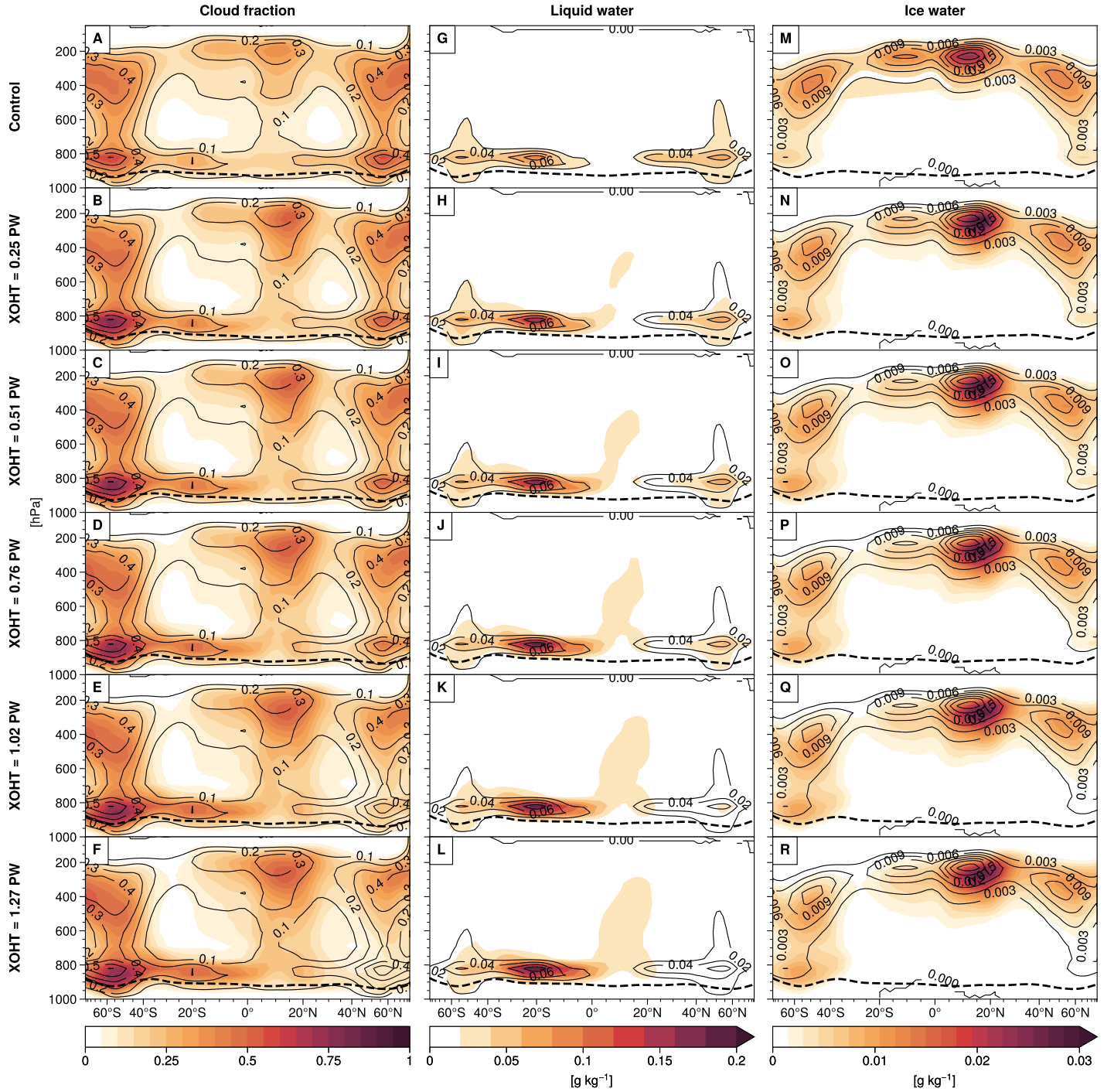
Figure 3. Mean cloud fraction (a-f), cloud liquid water content (g-l), and cloud ice content (m-r) across the experiments. Contour lines represent the control simulation for each variable. The dashed line represents the planetary boundary layer for each experiment.

Despite cooling, the SH has nearly invariant gradients in DSE and $L_v \cdot q$ and can thus maintain high poleward AHT. The NH sees weakening gradients in DSE; together with declining VL, this ultimately weakens diffusive processes and diminishes poleward AHT in the NH.

Strengthening SH trade winds increases turbulence, deepening the PBL and increasing upward moisture fluxes (see Supplementary Figure S2). In this way the conditions providing increasing SH subtropical low cloud cover may then also aid in tropospheric moistening, since growing the low cloud layer necessitates more detrainment of moist air into the troposphere. Thus the SH subtropics can dynamically more efficiently moisten the atmospheric column despite cooling, which may explain the marginal changes in column humidity gradients across the experiments (Figure 4i). More efficient upward moisture transport between the PBL and troposphere has been argued to play a role in the hydrological cycle in cold climates (Held and Soden, 2006).

3.2 Atmospheric heat transport responses

The ocean-atmosphere system works to reduce equator-to-pole temperature gradients through meridional heat transport (MHT); when one component of MHT is changed, other components tend to compensate for it to maximize poleward heat transport, a tendency known as Bjerknes compensation (Bjerknes, 1964). AHT follows this tendency in our simulations in two ways: by providing southward cross-equatorial heat transport via the Hadley circulation response (Held, 2001; Donohoe et al., 2013) to compensate for the northward XOHT, and by maintaining a constant poleward heat transport in the extratropics. The latter occurs asymmetrically between the hemispheres: NH extratropical AHT weakens with more XOHT, while SH extratropical AHT remains constant.

The methods of Shaw et al. (2022) provides a diagnostic tool for decomposing drivers of TE heat transport in the extratropics into contributions to the heat flux profile by surface fluxes, ASR, OLR, and nontransient circulation (which in our case is only MMC, due to the lack of stationary circulation). Increasing ASR at high latitudes works against TE, since energy input works against the energy deficit of the extratropics that TE reduces. In our simulation, NH cloud loss suppresses TE heat transport, since less energy import into the extratropics is needed, while SH cloud cover drives TE heat transport because the increases in cloud albedo reinforces the meridional heating gradient (see Supplementary Figure S3).

Clouds impact MHT via their radiative effects (Zelinka and Hartmann, 2012; Liu et al., 2017) and condensation, which provides latent heating (Fajber et al., 2023). Equation 3 can be calculated using clear-sky ASR and OLR to get the MHT implied by the clear-sky TOA radiation balance (MHT$_{\text{clear}}$). The difference between all- and clear-sky MHT give the effect of clouds on MHT, and since OHT is fixed, on AHT:

$$\text{AHT}_{\text{CRE}}(\varphi) \equiv \text{MHT}(\varphi) - \text{MHT}_{\text{clear}}(\varphi) - \text{OHT}(\varphi). \tag{9}$$

Condensation affects AHT by converting moisture into dry static energy (DSE) through latent heat release (Fajber et al., 2023); the magnitude that this has on AHT can be calculated using the meridional divergence of latent heat release, which we obtain using $\bullet \, (\varphi) = L_v \cdot P(\varphi)$ in equation (2):

$$\text{AHT}_{\text{LHR}}(\varphi) = 2\pi a^2 \int_{-\pi/2}^{\varphi} L_v \cdot \text{P}(\varphi) \cos(\varphi) \, d\varphi. \tag{10}$$

Figure 5j shows that AHT$_{\text{CRE}}$ increases southward MHT at low latitudes (up to ca 30°) and in the NH high latitudes with greater XOHT, aiding in southward cross-equatorial AHT. This is because clouds cool the NH low latitudes where the tropical maximum in cloud cover and
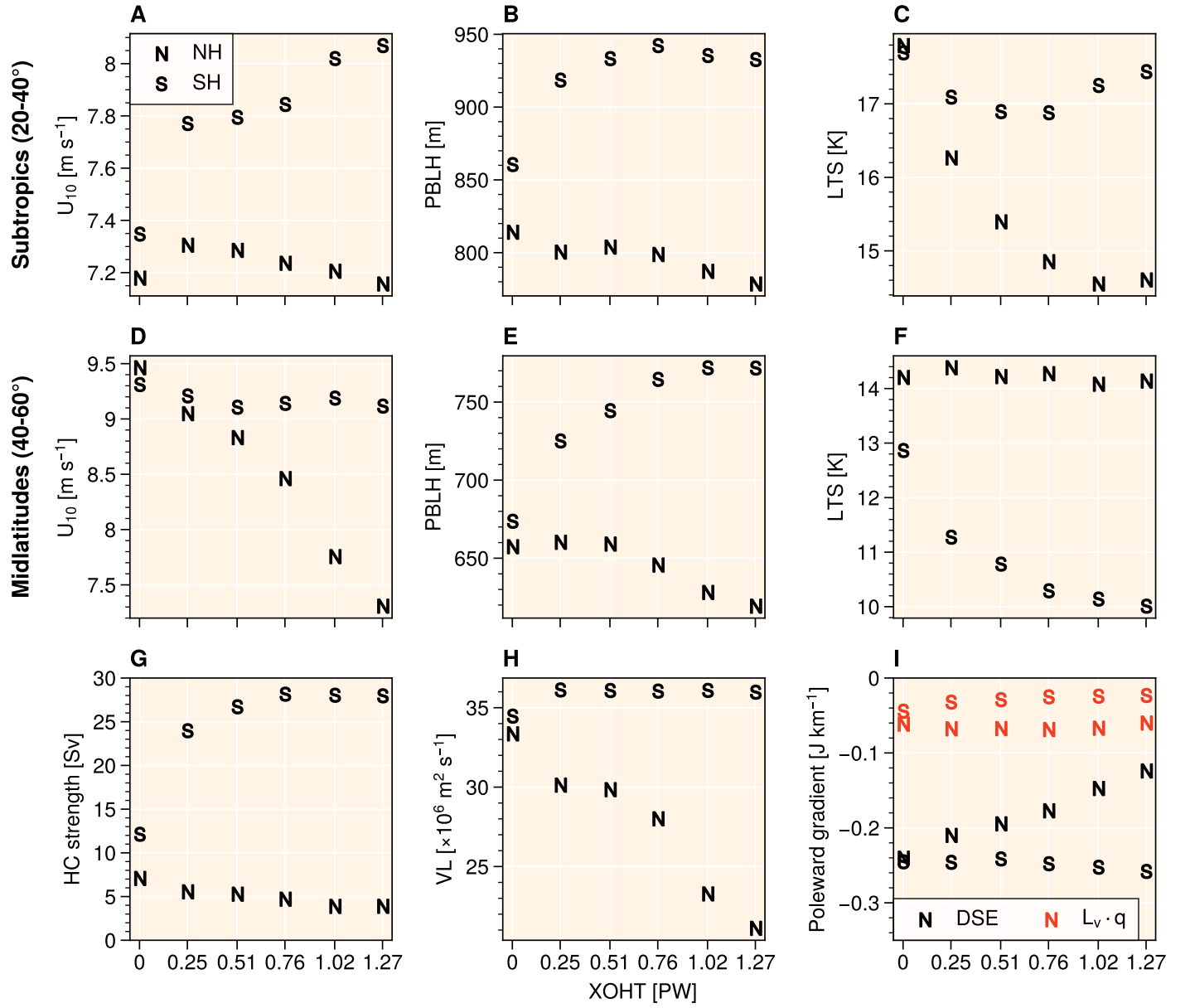
Figure 4. Area mean 10 m wind speed strengths (U_{10}), planetary boundary layer height (PBLH), and lower tropospheric stability (LTS) over the subtropics (top row) and midlatitudes (second row). Third row: g) the maximum overturning stream function strength of each hemisphere (where 1 Sv = 10^9 kg s^{-1}), h) eddy diffusivity scale VL averaged over 40-60° in each hemisphere, and i) poleward gradients of vertically intergrated dry static energy (DSE) and $L_v \cdot q$ averaged over 40-60° in each hemisphere.
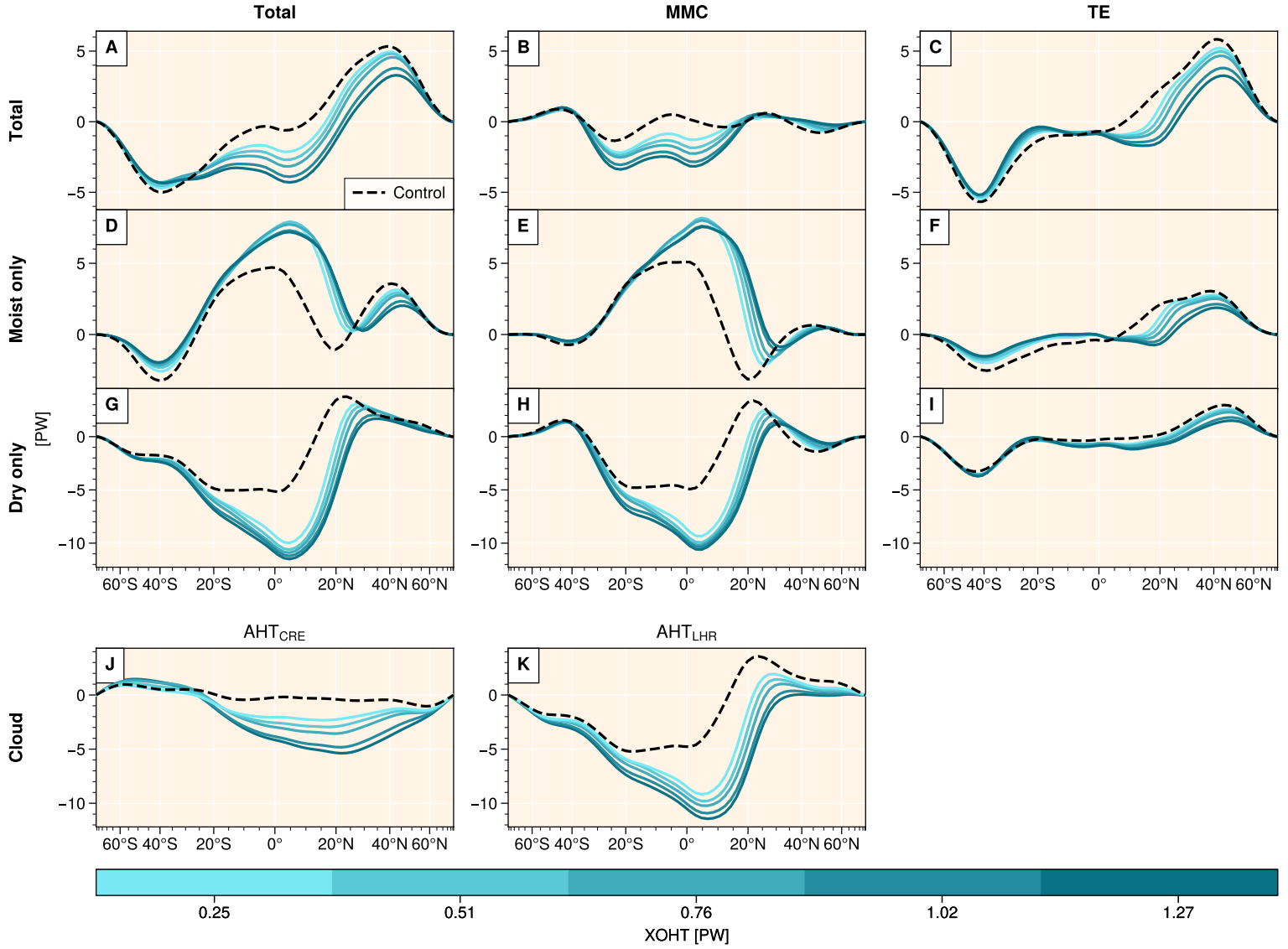
Figure 5. Total AHT (left column), heat transport by mean meridional circulation (MMC; middle column), and heat transport by transient eddies (TE; right column). Moist- and dry-only components of each are given in the second and third rows, respectively. Effects on AHT by j) cloud radiative effects (AHT_{CRE}) and k) latent heating (AHT_{LHR}) are given in the bottom row. The color denotes the strength of XOHT in the experiment.

ITCZ are located, reducing the interhemispheric heating gradient in the tropics, and cloud loss amplifies high-latitude heating, reducing the need for poleward AHT. These effects mirror the observed effect of CRE to increase southward MHT at all latitudes in satellite observations, which primarily occurs through albedo (Pearce and Bodas-Salcedo, 2023).

With increasing XOHT, AHT_{LHR} plays a diminishing role in poleward heat transport in the NH midlatitudes, while it strengthens AHT in the SH midlatitudes. The difference between dry AHT increases and moist AHT reductions in the SH midlatitudes is roughly equal to AHT_{LHR}, indicating that increasing condensation in the SH extratropics is contributing to maintaining high poleward AHT. However, increased condensation does not necessarily mean increased cloud cover, since condensate can precipitate almost instantaneously (factors affecting this will be explored in Section 3.3). At low latitudes, AHT_{LHR} increases southward AHT because of latent heating in the ITCZ, which provides DSE aloft to flow southward.

The sum effect of condensation and clouds on AHT follows Bjerknes compensation tendencies by weakening poleward AHT in the NH midlatitudes and strengthening poleward AHT in the SH midlatitudes. This is possible because gains in poleward AHT from LHR are larger than losses from CRE. This implies that the increasing extratropical SH cloud cover is compensating for reduced moist AHT with cooling by accelerating moisture cycling, increasing latent heating as well as time-average cloud cover. Between XOHT steps, changes in AHT_{LHR} are nearly proportional to AHT_{CRE} in the midlatitudes so that gains from increasing latent heat release are not outweighed by the losses in poleward heat transport through cloud radiative effects (see Supplementary Figure S3c-d).

3.3 Midlatitude moisture convergence

In the previous subsection, we described how increasing midlatitude cloud albedo with storm track activity works against poleward AHT. Cloud albedo is primarily determined by LWP, and average albedo for a given area is thus proportional to the average cloud condensate in a given area ($\overline{\text{LWP}} = f \cdot \text{LWP}$). $\overline{\text{LWP}}$ is in turn proportional to the convergence of moisture in the midlatitudes (P - E), thus:

$$\alpha \propto \overline{\text{LWP}} \propto \text{P} - \text{E}. \tag{11}$$

The moisture convergence framework (McCoy et al., 2020, 2022) can be useful to investigate the hemispheric differences in the relation between midlatitude clouds and moisture. Consistent with their relation across models (McCoy et al., 2020, 2022), $\overline{\text{LWP}}$ is to first order determined by P - E in our simulations (Figure 6a). Figure 6b shows that declining P primarily drives the reducing SH midlatitude moisture convergence with increasing XOHT, while increasing E primarily drives the increasing NH midlatitude moisture convergence.

The potential time-average amount of suspended cloud condensate for a given moisture convergence is proportional to the efficiency of condensate sources relative to their sinks:

$$\overline{\text{LWP}} \propto \frac{\text{CE}}{\text{PE}} \cdot (\text{P} - \text{E}), \tag{12}$$

where CE is the condensation efficiency (the rate of condensation proportional to the water vapor path WVP), and PE is the precipitation efficiency (the rate of precipitation proportional to the average amount of condensate):

$$\text{PE} = \frac{\text{P}}{\overline{\text{LWP}}}. \tag{13}$$

Since condensation must balance precipitation at steady state, we estimate CE using the ratio of precipitation to WVP:

$$CE = \frac{P}{WVP}. \tag{14}$$

Equation (12) states that when cloud condensate sources are larger relative to their sinks, there is on average more condensate accumulation in the atmosphere. Thus, a larger CE/PE yields a higher $\overline{LWP}$ and albedo for a given moisture convergence. These metrics yield diagnostics for cloud condensate accumulation in each hemisphere's midlatitudes, which are plotted in Figure 6c-d. In our simulations, the NH midlatitudes see increasing PE and marginal changes in CE, while the SH midlatitudes see increasing CE and no changes in PE. This implies that precipitation is remaining constantly proportional to $\overline{LWP}$ in the SH, while $\overline{LWP}$ for a given mean WVP is increasing.

To the first order, PE is controlled by the form of precipitation initiation, where convection yields a higher PE and large-scale precipitation is associated with low PE (Sui et al., 2007). The proportion of large scale to total P in the SH midlatitudes remains constant throughout the simulations, and the NH midlatitudes see increasingly more convective precipitation (see Supplementary Figure S4). This implies that processes determining PE in the SH midlatitudes do not change with increasing XOHT, and that changes in precipitation are determined by reduced moisture availability. The subtropics are the source of moisture and heat that eddies mix polewards, and thus moisture availability in the subtropics can affect moisture convergence and moist AHT in the midlatitudes. Thus the upward supply of moisture described in Section 3.1 may play a role in increasing SH midlatitude CE throughout the experiments.

To see if these tendencies in hemispheric differences in midlatitude moisture cycling mirror those of the real world, we look to observed ocean-only climatologies of precipitation from the Global Precipitation Climatology Project (GPCP; Adler et al. 2016) as well as water vapor path and cloud properties from the Clouds and Earth's Radiant Energy System Synoptic 1 Degree data set (CERES SYN1deg; NASA/LARC/SD/ASDC 2017). Grid cell area condensate is obtained from the Moderate Resolution Imaging Spectrometer (MODIS) instrument measurements of LWP and cloud fraction with $LWP \cdot f$. We find that observed hemispheric differences in these tendencies mirror those seen in our simulations. CE is 15.8% higher in the SH than the NH, while PE is 13.3% higher in the NH than the SH. The resulting CE/PE ratio is higher in the SH than the NH by 23.5%. Using another observational data set for $\overline{LWP}$–the Multisensor Advanced Climatology of Liquid Water Path (MAC-LWP; Elsaesser et al. 2017)–also leads to a 16.7% higher CE/PE ratio in the SH than NH, despite differences between NH and SH PE being more slight (3% higher in the NH) than in MODIS (Figure 6c-d). These differences, in agreement with previous findings, would suggest that some of the hemispheric asymmetry in midlatitude cloud cover responses to increasing northward XOHT arise from differences come from processes other than storm track intensity determining condensation and precipitation that resemble differences between different climate states (Zhao, 2014; McCoy et al., 2020).

4 DISCUSSION AND CONCLUSIONS

We find that most of the observed hemispheric asymmetries in cloud cover are qualitatively reproduced by a surface-forced hemispheric heating contrast induced by a mean northward cross-equatorial OHT. The mean northerly position of the ITCZ and maximum of tropical cloud cover is, as understood previously, a response of the Hadley circulation that enables southward cross-equatorial AHT to compensate for the hemispheric heat contrast. Our results suggest that extratropical asymmetries in cloud cover are linked to this tropical cloud asymmetry.
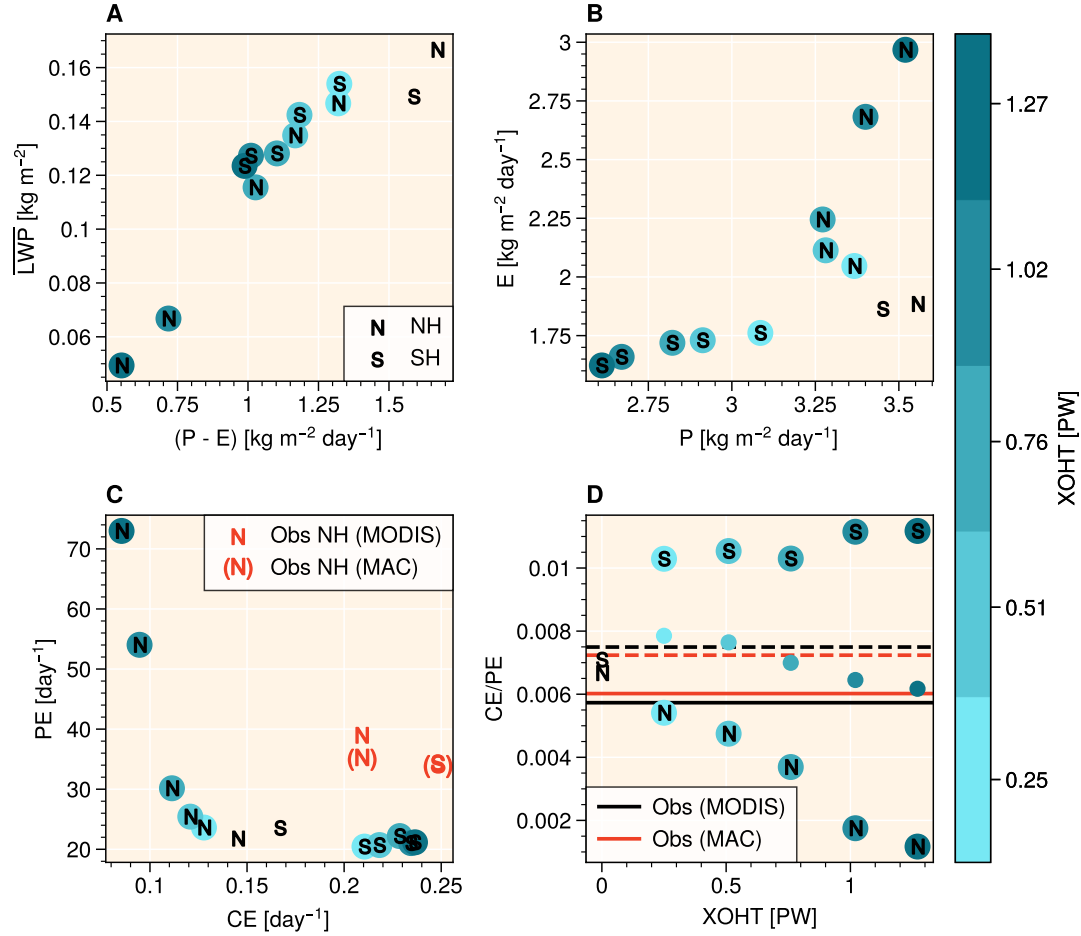
Figure 6. a) Midlatitude (40-60°) area-averaged condensate ($\overline{\mathrm{LWP}}$) plotted against moisture convergence (P - E) in our simulations. b) E plotted against P. c) Precipitation efficiency (PE) plotted against condensation efficiency (CE), with observational estimates (see text) for the NH and SH in red. Observational estimates made with MAC-LWP data are denoted by markers with parentheses. d) The CE/PE plotted as a function of cross-equatorial OHT in our forcings (XOHT). Colors represent the experiment. In d), horizontal lines represent estimates from observed climatologies, where solid lines represent the NH and dashed represent the SH. The red observational estimate lines denote those calculated with MAC-LWP.

Dynamically, the strengthening of the SH Hadley cell with Hadley circulation asymmetry causes stronger surface winds and large-scale subsidence in the subtropics, providing favorable conditions for LCC, and the SH storm track remains strong, while the NH storm track weakens. Given the relation between storm track intensity and albedo (McCoy et al., 2020; Hadas et al., 2023), this provides the midlatitude cloud asymmetry by reducing NH storm track cloud cover. Energetically, cloud responses to dynamic asymmetries propagate cooling and warming signals polewards in each hemisphere. The increase in SH subtropical LCC with Hadley asymmetry causes local cooling, limiting the amount of heat that can be transported polewards. Conversely, warming in the NH increases the efficiency of poleward AHT, first and foremost by increasing evaporation and thus moist AHT, reducing baroclinicity and thus storm track intensity. We also describe differences in the hydrological cycle of each hemispheres' midlatitudes that further contribute to hemispheric midlatitude cloud asymmetries.

Relating the clouds to cross-equatorial heat transport may offer insights into cloud radiative feedbacks from the perspective of their impacts on the energy balances of each hemisphere. Hemispheric differences in clouds may thus be able to provide valuable insights about cloud properties in different climate states and their responses to warming. However, the responses in our simulations give different feedbacks in each hemisphere, which results in nonlinear global responses to our OHT perturbations, ultimately yielding different global mean temperatures at equilibrium for the same energy balance and atmospheric composition. In other words, interhemispheric coupling makes it so that hemispheric differences are not perfect proxies for different climate states.

We describe processes determining the hemispheric asymmetry of global cloud cover to cross-equatorial OHT, providing a constraint for albedo symmetry-maintaining mechanisms, which must implicate ocean dynamics. The real-world analog capable of modulating OHT is provided by ocean meridional overturning circulation (MOC). MOC (and thus OHT) can change on relatively short timescales (Menary et al., 2020; Robson et al., 2022), making it a potential candidate for mediating hemispheric cloud asymmetries and maintaining hemispheric albedo symmetry. Furthermore, MOC is itself made possible by the arrangement of the continents (e.g. Talley 2008; Ferreira et al. 2018), which introduces complex dependencies between the clear-sky albedo asymmetry and the OHT forcing of global cloud cover.

Although polar climate is not studied here, a further key feature of the hemispheric differences in atmospheric responses seen in our experiments is the asymmetric impact on poleward AHT and polar cooling. Because poleward OHT becomes vanishingly small in polar latitudes, AHT is left to redistribute heat to the high polar regions. With an NH-brighter clear-sky albedo asymmetry in combination with NH ocean heat convergence, the polar warming provided by efficient poleward AHT in the NH would reduce ice cover and albedo, while increasing SH polar albedo. In a fully coupled climate, this would couple the hemispheric cloud asymmetries with polar temperature and albedo asymmetries and provide a mechanism for albedo symmetry maintenance. These atmospheric processes may also have been at play in polar climate oscillations in Earth's past, where cloud feedbacks stemming from midlatitude ocean warming signals occurring by MOC variability may have communicated polar climate signals between the hemispheres (Pedro et al., 2018; Thompson et al., 2019). Given the mid- and high latitudes' strong control on the hemispheric albedo symmetry (Jönsson and Bender, 2022; Jönsson and Bender, 2023), this would undoubtedly have driven changes to the symmetry.

In our simulations, positive cloud feedbacks provide hemispheric cloud asymmetries that amplify the energetic asymmetries imposed by ocean heat fluxes, which the atmosphere should be trying to reduce. We have detailed how atmospheric circulation responses that provide southward cross-

equatorial AHT lead to these hemispheric cloud asymmetries. If instead cloud feedbacks were negative, cloud responses would reduce the energetic contrast provided by the XOHT forcing, and less southward cross-equatorial AHT would be required. In other words, the resulting hemispheric cloud asymmetries work against the very heat transport that the atmospheric circulation provides to reduce heat gradients. Hemispheric albedo symmetry may then be explained by the tendency for the climate system to assume equilibrium states where positive radiative feedbacks–which albedo and SW cloud feedbacks likely are (Forster et al., 2021)–give a minimal contribution to the net hemispheric energy contrast. Albedo's minimal possible contribution to the hemispheric energy contrast would be zero given sufficient degrees of freedom to adjust the distribution of albedo. This explanation would provide further justification for the usefulness of the observed hemispheric albedo symmetry in understanding climate feedbacks, and inform constraints for symmetry-maintaining mechanisms.

CONTRIBUTIONS

ACKNOWLEDGMENTS

DATA AVAILABILITY

CERES SYN1deg data can be downloaded from https://ceres.larc.nasa.gov/data/, and GPCP data can be downloaded from https://psl.noaa.gov/data/gridded/data.gpcp.html. MAC-LWP data can be downloaded from https://climatesciences.jpl.nasa.gov/projects/cloudyboundary/index.html.

REFERENCES

Adler, R., Wang, J.-J., Sapiano, M., Huffman, G., Chiu, L., Xie, P. P., Ferraro, R., Schneider, U., Becker, A., Bolvin, D., Nelkin, E., and Gu, G. (2016). Global Precipitation Climatology Project (GPCP) Climate Data Record (CDR), Version 2.3 (Monthly).

Barry, L., Craig, G. C., and Thuburn, J. (2002). Poleward heat transport by the atmospheric heat engine. *Nature*, 415(6873):774–777.

Bender, F. A.-M., Engström, A., Wood, R., and Charlson, R. J. (2017). Evaluation of Hemispheric Asymmetries in Marine Cloud Radiative Properties. *Journal of Climate*, 30(11):4131 – 4147.

Bjerknes, J. (1964). Atlantic Air-Sea Interaction. volume 10 of *Advances in Geophysics*, pages 1–82. Elsevier.

Blanco, J. E., Caballero, R., Datseris, G., Stevens, B., Bony, S., Hadas, O., and Kaspi, Y. (2023). A Cloud-Controlling Factor Perspective on the Hemispheric Asymmetry of Extratropical Cloud Albedo. *Journal of Climate*, 36(6):1793 – 1804.

Bodas-Salcedo, A., Hill, P. G., Furtado, K., Williams, K. D., Field, P. R., Manners, J. C., Hyder, P., and Kato, S. (2016). Large Contribution of Supercooled Liquid Clouds to the Solar Radiation Budget of the Southern Ocean. *Journal of Climate*, 29(11):4213 – 4228.

Bodas-Salcedo, A., Williams, K. D., Field, P. R., and Lock, A. P. (2012). The Surface Downwelling Solar Radiation Surplus over the Southern Ocean in the Met Office Model: The Role of Midlatitude Cyclone Clouds. *Journal of Climate*, 25(21):7467 – 7486.

Ceppi, P., Hwang, Y.-T., Liu, X., Frierson, D. M. W., and Hartmann, D. L. (2013). The relationship between the ITCZ and the Southern Hemispheric eddy-driven jet. *Journal of Geophysical Research: Atmospheres*, 118(11):5136–5146.

D'Agostino, R. and Lionello, P. (2017). Evidence of global warming impact on the evolution of the Hadley Circulation in ECMWF centennial reanalyses. *Climate Dynamics*, 48(9):3047–3060.

Danabasoglu, G., Lamarque, J.-F., Bacmeister, J., Bailey, D. A., DuVivier, A. K., Edwards, J., Emmons, L. K., Fasullo, J., Garcia, R., Gettelman, A., Hannay, C., Holland, M. M., Large, W. G., Lauritzen, P. H., Lawrence, D. M., Lenaerts, J. T. M., Lindsay, K., Lipscomb, W. H., Mills, M. J., Neale, R., Oleson, K. W., Otto-Bliesner, B., Phillips, A. S., Sacks, W., Tilmes, S., van Kampenhout, L., Vertenstein, M., Bertini, A., Dennis, J., Deser, C., Fischer, C., Fox-Kemper, B., Kay, J. E., Kinnison, D., Kushner, P. J., Larson, V. E., Long, M. C., Mickelson, S., Moore, J. K., Nienhouse, E., Polvani, L., Rasch, P. J., and Strand, W. G. (2020). The Community Earth System Model Version 2 (CESM2). *Journal of Advances in Modeling Earth Systems*, 12(2):e2019MS001916. e2019MS001916 2019MS001916.

Datseris, G. and Stevens, B. (2021). Earth's albedo and its symmetry. *AGU Advances*, 2(3):e2021AV000440.

Davis, N. A. and Birner, T. (2019). Eddy Influences on the Hadley Circulation. *Journal of Advances in Modeling Earth Systems*, 11(6):1563–1581.

Diamond, M. S., Gristey, J. J., Kay, J. E., and Feingold, G. (2022). Anthropogenic aerosol and cryosphere changes drive Earth's strong but transient clear-sky hemispheric albedo asymmetry. *Communications Earth & Environment*, 3(1):206.

Donohoe, A., Marshall, J., Ferreira, D., and Mcgee, D. (2013). The Relationship between ITCZ Location and Cross-Equatorial Atmospheric Heat Transport: From the Seasonal Cycle to the Last Glacial Maximum. *Journal of Climate*, 26(11):3597 – 3618.

Elsaesser, G. S., O'Dell, C. W., Lebsock, M. D., Bennartz, R., Greenwald, T. J., and Wentz, F. J. (2017). The Multisensor Advanced Climatology of Liquid Water Path (MAC-LWP). *Journal of Climate*, 30(24):10193 – 10210.

Fajber, R., Donohoe, A., Ragen, S., Armour, K. C., and Kushner, P. J. (2023). Atmospheric heat transport is governed by meridional gradients in surface evaporation in modern-day Earth-like climates. *Proceedings of the National Academy of Sciences*, 120(25):e2217202120.

Ferreira, D., Cessi, P., Coxall, H. K., de Boer, A., Dijkstra, H. A., Drijfhout, S. S., Eldevik, T., Harnik, N., McManus, J. F., Marshall, D. P., Nilsson, J., Roquet, F., Schneider, T., and Wills, R. C. (2018). Atlantic-Pacific Asymmetry in Deep Water Formation. *Annual Review of Earth and Planetary Sciences*, 46(1):327–352.

Forster, P., Storelvmo, T., Armour, K., Collins, W., Dufresne, J. L., Frame, D., Lunt, D. J., Mauritsen, T., Palmer, M. D., Watanabe, M., Wild, M., and Zhang, H. (2021). The Earth's Energy Budget, Climate Feedbacks, and Climate Sensitivity. In Masson-Delmotte, V., Zhai, P., Pirani, A., Connors, S. L., Péan, C., Berger, S., Caud, N., Chen, Y., Goldfarb, L., Gomis, M. I., Huang, M., Leitzell, K., Lonnoy, E., Matthews, J. B. R., Maycock, T. K., Waterfield, T., Yelekçi, O., Yu, R., and Zhou, B., editors, *Climate Change 2021: The Physical Science Basis. Contribution of Working Group I to the Sixth Assessment Report of the Intergovernmental Panel on Climate Change*, book section 7, pages 923–1054. Cambridge University Press, Cambridge, United Kingdom and New York, NY, USA.

Green, B., Marshall, J., and Campin, J.-M. (2019). The 'sticky' ITCZ: ocean-moderated ITCZ shifts. *Climate Dynamics*, 53(1):1–19.

Hadas, O., Datseris, G., Blanco, J., Bony, S., Caballero, R., Stevens, B., and Kaspi, Y. (2023). The role of baroclinic activity in controlling Earth's albedo in the present and future climates. *Proceedings of the National Academy of Sciences*, 120(5):e2208778120.

Held, I. M. (2001). The Partitioning of the Poleward Energy Transport between the Tropical Ocean and Atmosphere. *Journal of the Atmospheric Sciences*, 58(8):943 – 948.

Held, I. M. and Soden, B. J. (2006). Robust Responses of the Hydrological Cycle to Global Warming. *Journal of Climate*, 19(21):5686 – 5699.

Jönsson, A. R. and Bender, F. A.-M. (2023). The implications of maintaining Earth's hemispheric albedo symmetry for shortwave radiative feedbacks. *Earth System Dynamics*, 14(2):345–365.

Jönsson, A. and Bender, F. A.-M. (2022). Persistence and Variability of Earth's Interhemispheric Albedo Symmetry in 19 Years of CERES EBAF Observations. *Journal of Climate*, 35(1):249 – 268.

Kang, S. M., Held, I. M., Frierson, D. M. W., and Zhao, M. (2008). The Response of the ITCZ to Extratropical Thermal Forcing: Idealized Slab-Ocean Experiments with a GCM. *Journal of Climate*, 21(14):3521 – 3532.

Kang, S. M., Seager, R., Frierson, D. M. W., and Liu, X. (2015). Croll revisited: Why is the northern hemisphere warmer than the southern hemisphere? *Climate Dynamics*, 44(5):1457–1472.

Klein, S. A., Hall, A., Norris, J. R., and Pincus, R. (2017). Low-Cloud Feedbacks from Cloud-Controlling Factors: A Review. *Surveys in Geophysics*, 38(6):1307–1329.

Liu, C., Allan, R. P., Mayer, M., Hyder, P., Loeb, N. G., Roberts, C. D., Valdivieso, M., Edwards, J. M., and Vidale, P.-L. (2017). Evaluation of satellite and reanalysis-based global net surface energy flux and uncertainty estimates. *Journal of Geophysical Research: Atmospheres*, 122(12):6250–6272.

Loeb, N. G., Wang, H., Cheng, A., Kato, S., Fasullo, J. T., Xu, K.-M., and Allan, R. P. (2016). Observational constraints on atmospheric and oceanic cross-equatorial heat transports: revisiting the precipitation asymmetry problem in climate models. *Climate Dynamics*, 46(9):3239–3257.

McCoy, D. T., Field, P., Bodas-Salcedo, A., Elsaesser, G. S., and Zelinka, M. D. (2020). A Regime-Oriented Approach to Observationally Constraining Extratropical Shortwave Cloud Feedbacks. *Journal of Climate*, 33(23):9967 – 9983.

McCoy, D. T., Field, P., Frazer, M. E., Zelinka, M. D., Elsaesser, G. S., Mülmenstädt, J., Tan, I., Myers, T. A., and Lebo, Z. J. (2022). Extratropical Shortwave Cloud Feedbacks in the Context of the Global Circulation and Hydrological Cycle. *Geophysical Research Letters*, 49(8):e2021GL097154. e2021GL097154 2021GL097154.

Menary, M. B., Robson, J., Allan, R. P., Booth, B. B. B., Cassou, C., Gastineau, G., Gregory, J., Hodson, D., Jones, C., Mignot, J., Ringer, M., Sutton, R., Wilcox, L., and Zhang, R. (2020). Aerosol-Forced AMOC Changes in CMIP6 Historical Simulations. *Geophysical Research Letters*, 47(14):e2020GL088166. e2020GL088166 2020GL088166.

Myers, T. A. and Norris, J. R. (2015). On the Relationships between Subtropical Clouds and Meteorology in Observations and CMIP3 and CMIP5 Models. *Journal of Climate*, 28(8):2945 – 2967.

NASA/LARC/SD/ASDC (2017). CERES and GEO-Enhanced TOA, Within-Atmosphere and Surface Fluxes, Clouds and Aerosols Monthly Terra-Aqua Edition4A.

Neale, R. and Hoskins, B. (2000). A standard test for AGCMs including their physical parametrizations: I: The proposal. *Atmospheric Science Letters*, 1(2):101–107.

Nuijens, L. and Stevens, B. (2012). The influence of wind speed on shallow marine cumulus convection. *Journal of the Atmospheric Sciences*, 69(1):168 – 184.

Pearce, F. A. and Bodas-Salcedo, A. (2023). Implied Heat Transport from CERES Data: Direct Radiative Effect of Clouds on Regional Patterns and Hemispheric Symmetry. *Journal of Climate*, 36(12):4019 – 4030.

Pedro, J. B., Jochum, M., Buizert, C., He, F., Barker, S., and Rasmussen, S. O. (2018). Beyond the bipolar seesaw: Toward a process understanding of interhemispheric coupling. *Quaternary Science Reviews*, 192:27–46.

Roach, L. A., Eisenman, I., Wagner, T. J. W., and Donohoe, A. (2023). Asymmetry in the Seasonal Cycle of Zonal-Mean Surface Air Temperature. *Geophysical Research Letters*, 50(10):e2023GL103403. e2023GL103403 2023GL103403.

Robson, J., Menary, M. B., Sutton, R. T., Mecking, J., Gregory, J. M., Jones, C., Sinha, B., Stevens, D. P., and Wilcox, L. J. (2022). The Role of Anthropogenic Aerosol Forcing in the 1850–1985 Strengthening of the AMOC in CMIP6 Historical Simulations. *Journal of Climate*, 35(20):6843 – 6863.

Rugenstein, M. and Hakuba, M. (2023). Connecting hemispheric asymmetries of planetary albedo and surface temperature. *Geophysical Research Letters*, 50(6):e2022GL101802.

Schiro, K. A., Su, H., Ahmed, F., Dai, N., Singer, C. E., Gentine, P., Elsaesser, G. S., Jiang, J. H., Choi, Y.-S., and David Neelin, J. (2022). Model spread in tropical low cloud feedback tied to overturning circulation response to warming. *Nature Communications*, 13(1):7119.

Shaw, T. A., Miyawaki, O., and Donohoe, A. (2022). Stormier Southern Hemisphere induced by topography and ocean circulation. *Proceedings of the National Academy of Sciences*, 119(50):e2123512119.

Singh, M. S. and Kuang, Z. (2016). Exploring the Role of Eddy Momentum Fluxes in Determining the Characteristics of the Equinoctial Hadley Circulation: Fixed-SST Simulations. *Journal of the Atmospheric Sciences*, 73(6):2427 – 2444.

Stephens, G. L., O'Brien, D., Webster, P. J., Pilewski, P., Kato, S., and Li, J.-l. (2015). The albedo of earth. *Reviews of Geophysics*, 53(1):141–163.

Stevens, B. and Schwartz, S. E. (2012). Observing and Modeling Earth's Energy Flows. *Surveys in Geophysics*, 33(3):779–816.

Sui, C.-H., Li, X., and Yang, M.-J. (2007). On the Definition of Precipitation Efficiency. *Journal of the Atmospheric Sciences*, 64(12):4506 – 4513.

Talley, L. D. (2008). Freshwater transport estimates and the global overturning circulation: Shallow, deep and throughflow components. *Progress in Oceanography*, 78(4):257–303.

Thompson, A. F., Hines, S. K., and Adkins, J. F. (2019). A Southern Ocean Mechanism for the Interhemispheric Coupling and Phasing of the Bipolar Seesaw. *Journal of Climate*, 32(14):4347 – 4365.

Vergara-Temprado, J., Miltenberger, A. K., Furtado, K., Grosvenor, D. P., Shipway, B. J., Hill, A. A., Wilkinson, J. M., Field, P. R., Murray, B. J., and Carslaw, K. S. (2018). Strong control of Southern Ocean cloud reflectivity by ice-nucleating particles. *Proceedings of the National Academy of Sciences*, 115(11):2687–2692.

Voigt, A., Stevens, B., Bader, J., and Mauritsen, T. (2013). The observed hemispheric symmetry in reflected shortwave irradiance. *Journal of Climate*, 26(2):468–477.

Voigt, A., Stevens, B., Bader, J., and Mauritsen, T. (2014). Compensation of Hemispheric Albedo Asymmetries by Shifts of the ITCZ and Tropical Clouds. *Journal of Climate*, 27(3):1029 – 1045.

Walker, C. C. and Schneider, T. (2006). Eddy Influences on Hadley Circulations: Simulations with an Idealized GCM. *Journal of the Atmospheric Sciences*, 63(12):3333 – 3350.

Zelinka, M. D. and Hartmann, D. L. (2012). Climate Feedbacks and Their Implications for Poleward Energy Flux Changes in a Warming Climate. *Journal of Climate*, 25(2):608 – 624.

Zelinka, M. D., Zhou, C., and Klein, S. A. (2016). Insights from a refined decomposition of cloud feedbacks. *Geophysical Research Letters*, 43(17):9259–9269.

Zhao, M. (2014). An Investigation of the Connections among Convection, Clouds, and Climate Sensitivity in a Global Climate Model. *Journal of Climate*, 27(5):1845 – 1862.